

Temperature-Induced Structural Reorganization of W-Doped $\text{Ba}_{0.5}\text{Sr}_{0.5}\text{Co}_{0.8}\text{Fe}_{0.2}\text{O}_{3-\delta}$ Composite Membranes for Air Separation

Guanghu He,^{†,‡,§} Qianqian Lan,^{§,||,#} Yoo Jung Sohn,[‡] Stefan Baumann,[‡] Rafal Dunin-Borkowski,[§] Wilhelm A. Meulenber,^{*,‡,⊥} and Heqing Jiang^{*,†,⊥}

[†]Qingdao Key Laboratory of Functional Membrane Material and Membrane Technology, Qingdao Institute of Bioenergy and Bioprocess Technology, Chinese Academy of Sciences, 266101 Qingdao, China

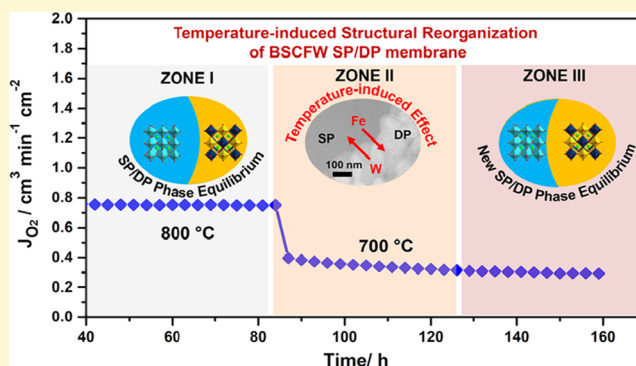
[‡]Institute of Energy and Climate Research (IEK-1) and [§]Ernst Ruska-Centre for Microscopy and Spectroscopy with Electrons and Peter Grünberg Institute 5 (PGI-5), Forschungszentrum Jülich, 52425 Jülich, Germany

^{||}School of Materials Science and Engineering, Tsinghua University, 100084 Beijing, China

[⊥]Faculty of Science and Technology, Inorganic Membranes, The University of Twente, 7500 AE Enschede, The Netherlands

Supporting Information

ABSTRACT: The practical use of $\text{Ba}_{0.5}\text{Sr}_{0.5}\text{Co}_{0.8}\text{Fe}_{0.2}\text{O}_{3-\delta}$ (BSCF) prototypical oxygen-transport membrane for air separation is currently hampered by the decomposition of the cubic perovskite into a variant with hexagonal stacking at intermediate temperatures of ≤ 850 °C, which impairs the oxygen transport. Here, we report the development of a W-doped BSCF composite that contains Fe-rich single perovskite (SP) and W-rich double perovskite (DP) phases with different crystallographic parameters. In contrast to BSCF, the BSCFW SP/DP composite maintains its cubic structure at 800 °C for 200 h, demonstrating its structural stability at intermediate temperatures. We use X-ray diffraction, scanning electron microscopy, and high-resolution transmission electron microscopy to show that the enhanced phase stability of the composite is associated with a temperature-induced SP–DP dynamic interaction, which involves W and Fe interdiffusion between the SP and DP phases, dynamically adjusting the chemical composition and limiting structural distortion and new phase formation. The composite exhibits a stable permeation performance in the oxygen-transport membrane during over 150 h operation at 800 and 700 °C, confirming the potential of intermediate-temperature oxygen-transport membranes for air separation and providing insight for designing thermally stable composite oxides.



INTRODUCTION

In the past decades, perovskite-type oxygen-transport membrane (OTM) materials have attracted research and commercial interest for use as oxygen pumps, catalytic membrane reactors, and cathodes in solid oxide fuel cells (SOFCs) owing to their mixed electronic–ionic conductivity at elevated temperature.^{1–5} $\text{Ba}_{0.5}\text{Sr}_{0.5}\text{Co}_{0.8}\text{Fe}_{0.2}\text{O}_{3-\delta}$ (BSCF) is a prototypical example of a high-performance membrane material, whose oxygen stoichiometry ($3 - \delta$) ranged from 2.54 at 100 °C to 2.36 at 900 °C.⁶ As an OTM with a thickness of 70 μm , it exhibited an oxygen permeation flux of approximately $5 \text{ cm}^3 \text{ min}^{-1} \text{ cm}^{-2}$ under an air/argon oxygen partial pressure gradient at 900 °C,⁷ satisfying the permeation flux of $\geq 1.0 \text{ cm}^3 \text{ min}^{-1} \text{ cm}^{-2}$, which is required for practical applications.⁸ To avoid the construction and durability problems that accompany the high operating temperatures of BSCF, it is desirable to lower the operating temperature to below 900 °C. However, severe performance degradation occurs at intermediate temperatures (IT-OTM, 500–850 °C)

because of poor thermodynamic stability of the cubic BSCF phase, leading to the partial decomposition of the cubic to the hexagonal phase and/or to $\text{Ba}_{n+1}\text{Co}_n\text{O}_{3n+3}$ phases,^{9–12} thus preventing practical use.

To address this issue, scientists have artificially modified the composition of the BSCF material by substituting Co or Fe by foreign cations such as Ti^{4+} ,¹³ Zr^{4+} ,^{14,15} Y^{3+} ,^{16,17} or Nb^{5+} .¹⁸ By using such a doping strategy, the phase stability of the BSCF perovskite at intermediate temperatures (500–850 °C) can be improved to some extent, albeit always at the expense of oxygen permeability. Little attention has been paid to study the reason for this “trade-off” between stability and permeability, which is always associated with the stabilization of the foreign-cation-doped BSCF perovskite at intermediate temperatures.¹⁹ Liu et al. ascribed the phase stability of the Y- or Ce-doped

Received: June 6, 2019

Revised: August 22, 2019

Published: August 22, 2019

BSCF at 600 °C to the formation of nanoparticle roadblocks, which inhibit the heterogeneous nucleation and new phase formation, at grain boundaries.²⁰ The suppression of cubic phase decomposition in the B-site Nb-doped BSCF after long-term annealing at 750 °C was explained using a Goldschmidt tolerance factor, with the large ionic radius of Nb⁵⁺ favoring the perovskite structure formation.¹⁸ Improved stability in the Zr-doped BSCF was attributed to the stabilization of the neighboring oxygen octahedra and an increase in the metal–oxygen bonding energy.²¹ The stabilization mechanism of the B-site cation-doped BSCF is therefore expected to be complex and likely to involve steric hindrance along grain boundaries, microstructure reconstruction, and energetic stability of cubic structure at intermediate temperatures (i.e., 500–850 °C).

Rosseinsky et al. recently found that the substitution of W⁶⁺ on the octahedral B-site of a Ba_{0.5}Sr_{0.5}Co_{0.8}Fe_{0.2}O_{3-δ} porous cathode in SOFCs resulted in a symmetry change, which was associated with the formation of single-perovskite (ABO₃, SP) and double-perovskite (A₂B₂O₆, DP) phases. Such a self-assembled BSCFW composite porous electrode material was reported to have high structural stability at 750 °C.²² In addition, it exhibited a very low area specific resistance as a porous electrode layer, resulting in high electrochemical activity for superior SOFC and oxygen evolution reaction performances.^{23,24} Wang et al. prepared a coexisting dual-phase composite ceramic consisting of BaCe_{0.85}Fe_{0.15}O_{3-δ} and BaCe_{0.15}Fe_{0.85}O_{3-δ} based on the auto-demixing of a single BaCe_{0.5}Fe_{0.5}O₃ precursor.²⁵ The two constituent phases were thermochemically stable and compatible with each other, with high hydrogen permeation performance below 850 °C. Based on these studies, this self-assembly concept is also thought to be applicable for the development of new oxygen-transport membranes with a high chemical and structural stability for air separation at intermediate temperatures.

Here, we report the development of new oxygen-transport membrane composites, which have the nominal composition Ba_{0.5}Sr_{0.5}(Co_{0.8}Fe_{0.2})_{1-x}W_xO_{3-δ} (BSCFW) and contain single-perovskite (SP) and double-perovskite (DP) phases with the same chemical elements but uneven Fe/W elemental distributions and different crystallographic parameters. In contrast to BSCF, the BSCFW SP/DP composite membrane material has a much higher structural stability at 800 °C due to temperature-induced W and Fe elemental interdiffusion between the SP and DP microstructures, which dynamically adjust their chemical compositions to adopt cubic symmetry and to reach a new phase equilibrium state. As a result of this temperature-induced structural reorganization, the BSCFW SP/DP composite membranes exhibit a stable oxygen separation performance at 700 and 800 °C, making them suitable for intermediate-temperature oxygen-transport membranes and providing insight into the design of thermally stable materials.

EXPERIMENTAL SECTION

Synthesis of BSCFW Powders and Membranes. High-purity (>99.5%) Ba, Sr, Co, and Fe metal nitrates and ammonium tungstate (Merck, Sigma Chemical) were used to prepare Ba_{0.5}Sr_{0.5}(Co_{0.8}Fe_{0.2})_{1-x}W_xO_{3-δ} (BSCFW, $x = 0, 0.05, 0.1, 0.2, 0.3,$ and 0.35) composite oxides via a combined ethylenediamine tetraacetic acid and citrate complex method.²⁶ The resulting powders were calcined at 950 °C for 10 h and then pressed into disks under a pressure of 30 MPa. The disks were sintered at 1150–1300 °C for 10 h to become gas-tight BSCFW membranes with 15.4 mm diameters and 1 mm thickness.

Characterization of Membrane Materials. The BSCFW composite membrane materials were characterized for their phase purity and structure using X-ray diffraction (XRD). Patterns were recorded from all BSCFW composite membrane materials in the 2θ range from 10 to 80° with a Bruker D4 endeavor device using a Cu Kα radiation. A high-temperature XRD measurement of BSCFW0.35 was also performed using the Cu Kα radiation with an Empyrean (Malvern Panalytica, The Netherlands) equipped with an HTK 1200 N high-temperature chamber (Anton Paar GmbH), with steps of 100 °C at a 5 °C min⁻¹ heating rate in an ambient atmosphere between 25 and 1000 °C. The acquisition time for each diffractogram was approximately 40 min. For quantitative analysis of the SP and DP phases in the BSCFW composite, Rietveld structure refinement of the XRD data was carried out using TOPAS software (Bruker AXS). Microstructure analysis of the as-prepared membrane materials was performed using scanning electron microscopy (SEM, Zeiss Merlin). A scanning transmission electron microscope (STEM) was performed on cross-sectional specimens prepared using focused ion beam (FIB) milling in an FEI Helios Nanolab 400s dual-beam system. The samples were further polished using a 500 eV Ar ion beam (Fischione Nanomill, model 1040) to remove the damaged layers introduced by FIB milling. High-angle annular dark-field (HAADF) STEM and energy-dispersive X-ray spectroscopy (EDX) mapping were performed in an FEI Titan G2 80-200 ChemiSTEM microscope equipped with a high-brightness field emission gun, a probe C_s corrector, and a super-X EDX system.

Oxygen Permeation Measurements. Oxygen permeation measurements were performed using a laboratory-scale quartz apparatus and a mass spectrometer, which is described elsewhere.²⁷ Disk-shape BSCFW membranes with a thickness of 1 mm were sealed onto a glass tube with two Au rings. Synthetic air was applied to one side of the membranes with a flow rate of 250 cm³ min⁻¹. On the other side, high-purity argon as a carrier gas was introduced with a flow rate of 50 cm³ min⁻¹. Gas flow rates were controlled using gas mass flow controllers (Bronkhorst, Germany). The permeated gas, being a mixture of argon and permeated oxygen, was analyzed using a mass spectrometer (Omnistar, Pfeiffer Vacuum). The nitrogen concentration in the permeated gas was measured to evaluate the relative leakage of oxygen according to the feed synthetic air. The leakage was typically below 1 % for all measurements, and the oxygen permeation fluxes were corrected by subtracting the oxygen leakage.

RESULTS AND DISCUSSION

Phase Composition of BSCFW Composites. Figure 1a shows the room-temperature XRD patterns recorded for the as-prepared Ba_{0.5}Sr_{0.5}(Co_{0.8}Fe_{0.2})_{1-x}W_xO_{3-δ} (BSCFW) oxides calcined at 950 °C for 10 h. When the doping content of W in BSCF was below 0.1 (i.e., BSCF and BSCFW0.05), the oxides were crystallized in single cubic perovskite structures without additional peaks, in accordance with previous studies.²⁸ On increasing the doping of W to 0.1 (i.e., BSCFW0.1), characteristic peaks of the double perovskite (DP) appeared, revealing that BSCFW0.1 becomes a SP–DP coexisting composite oxide. The DP peaks could be assigned to Ba₂CoWO₆ (JCPDS no. 74-1605) and/or Sr₂FeWO₆ (JCPDS no. 85-1957) with a cubic fluorite structure. The crystal structures of the single-perovskite and double-perovskite phases are shown in Figure 1b,c. After a quantitative Rietveld phase analysis, the mass percentages of SP and DP in this coexisting dual-phase system are approximately 75 and 25%, respectively (Table 1), indicating a thermodynamic equilibrium state of the SP and DP phases in BSCFW0.1 at room temperature. With continued rise in the W doping amount, the XRD peak intensities of the DP phase increased gradually and became dominant in BSCFW, reaching ~79 wt % when the W doping content was 0.35 (i.e., BSCFW0.35).

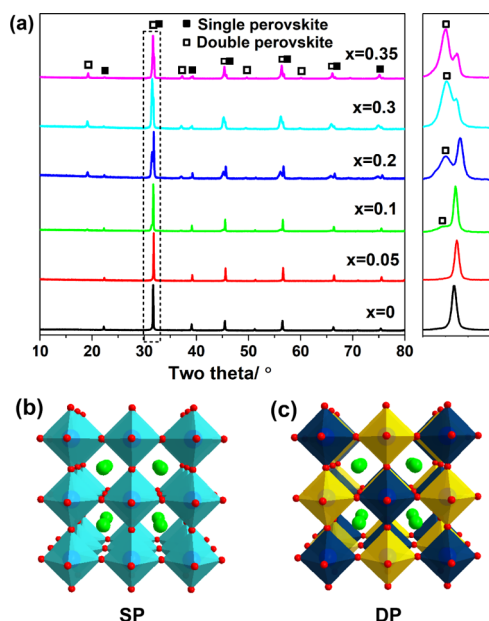


Figure 1. (a) X-ray diffraction data recorded for the as-prepared $\text{Ba}_{0.5}\text{Sr}_{0.5}(\text{Co}_{0.8}\text{Fe}_{0.2})_{1-x}\text{W}_x\text{O}_{3-\delta}$ (BSCFW, $x = 0, 0.05, 0.1, 0.2, 0.3, 0.35$) oxides that had been calcined at 950°C for 10 h. (b, c) Single-perovskite and double-perovskite crystal structures.

Table 1. Mass Ratios of Single-Perovskite (SP) and Double-Perovskite (DP) Phases in BSCFW Composites at Room Temperature

	ratio of SP	ratio of DP
BSCF	100	0
BSCFW0.05	<100	undetected
BSCFW0.1	75	25
BSCFW0.2	47	53
BSCFW0.3	24	76
BSCFW0.35	21	79

The original results of the quantitative Rietveld analysis, which were obtained using a commercial TOPAS software package for the BSCFW SP/DP composites, are provided in the Supporting Information (Figure S1).

The morphologies of the BSCFW SP/DP composites were characterized using SEM, as shown in Figure 2. For BSCF

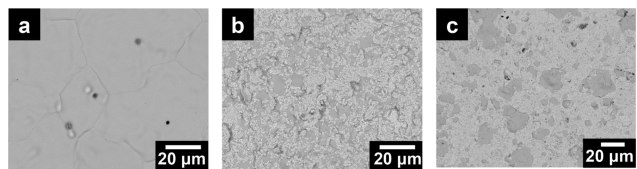


Figure 2. SEM images of the (a) as-prepared BSCF, (b) BSCFW0.2, and (c) BSCFW0.35 membrane surfaces.

without W doping, no additional phases (other than the cubic single perovskite) were found, in accordance with the XRD pattern shown in Figure 1a. For W-doped BSCF with a doping content of $x = 0.2$ (i.e., BSCFW0.2), the surface became rough and contained larger and smaller grains. The surface of BSCFW0.35 was even rougher, with a smaller proportion of the surface area covered by large grains and a corresponding increase in surface area covered by small grains. Based on the XRD peaks and mass ratios of the SP and DP phases in the

BSCFW oxides shown in Figure 1 and Table 1, the smaller grains in the SEM images of BSCFW0.2 and BSCFW0.35 were identified as DP and the larger grains as SP.

Based on these results, we infer that the precursor $\text{Ba}_{0.5}\text{Sr}_{0.5}(\text{Co}_{0.8}\text{Fe}_{0.2})_{1-x}\text{W}_x\text{O}_{3-\delta}$ autoseparates into SP and DP phases and forms a coexisting dual-phase system after one-step calcination. An increase in the W content of the BSCFW precursor results in a decrease in the concentration of the SP phase, with a corresponding increase in the concentration of the DP phase, suggesting an inter-relationship between W doping and the phase equilibrium of the SP–DP coexisting dual-phase system at room temperature.

Intermediate-Temperature-Stable BSCFW SP/DP Composite. According to previous studies,^{9,11} phase decomposition of the cubic BSCF perovskite in an ambient atmosphere occurs in an intermediate temperature window between 500 and 850°C . To evaluate the phase stability of the BSCFW SP/DP composite system at intermediate temperatures, all of the as-prepared BSCFW oxides were annealed at 800°C for 200 h and analyzed using XRD, as shown in Figure 3. In agreement with previous observations,¹⁰ characteristic

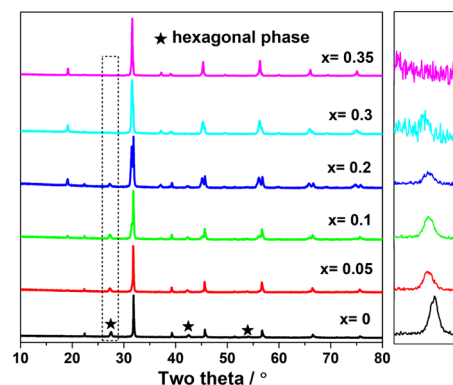


Figure 3. X-ray diffraction data from $\text{Ba}_{0.5}\text{Sr}_{0.5}(\text{Co}_{0.8}\text{Fe}_{0.2})_{1-x}\text{W}_x\text{O}_{3-\delta}$ (BSCFW, $x = 0, 0.05, 0.1, 0.2, 0.3, 0.35$) after thermal exposure at 800°C for 200 h in ambient atmosphere.

reflections corresponding to hexagonal phases with a 2H stacking sequence (space group $P63/mmc$) were observed at approximately $27.5, 42.6,$ and 54.2° (2θ) in the XRD pattern of the nondoped BSCF, indicating the phase decomposition of the BSCF cubic perovskite. After doping BSCF with W to form a SP/DP dual-phase assemblage, Figure 3 shows that the peak intensity of the hexagonal phase gradually becomes weaker with increasing W content. In particular, the hexagonal phase in the BSCFW0.35 composite is not detectable, indicating that the BSCFW SP/DP composite oxide has a high phase stability at intermediate temperatures.

To reveal the stabilization mechanism of the BSCFW SP/DP composite at intermediate temperature, high-resolution transmission electron microscopy and energy-dispersive X-ray spectroscopy (EDX) of BSCFW0.35 were performed. As shown in Figure 4a, different grains in BSCFW0.35 are recognizable as bright and dark crystallites in an HAADF-STEM image, as well as in low-magnification TEM images (Figure S2, Supporting Information). Figure 4b shows a high-resolution HAADF-STEM image recorded from the region marked by a red rectangle in Figure 4a, which shows an intimately mixed two-phase microstructure of SP and DP without intermediate phases at their interfaces, indicating

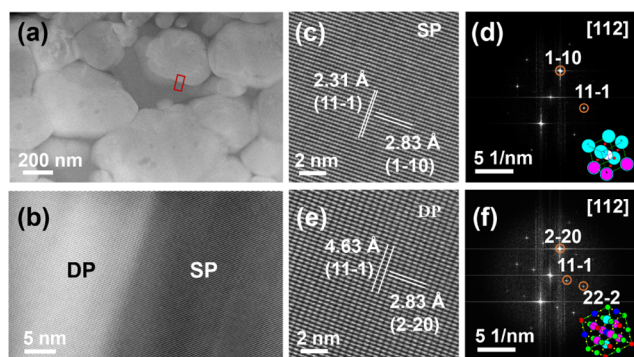


Figure 4. Microstructure of BSCFW0.35. (a) Low-magnification HAADF-STEM image of BSCFW0.35. (b) HAADF-STEM image of an interface between DP and SP crystallites, recorded from the marked region in (a). (c, d) High-resolution HAADF-STEM image of the SP phase and its Fourier transform. (e, f) High-resolution HAADF-STEM image of the DP phase and its Fourier transform.

excellent compatibility between the SP and DP phases. Figure 4c,e shows the representative high-resolution HAADF-STEM images of the SP and DP phases. The interplanar distances in SP are measured to be 2.83 and 2.31 Å, which are consistent with the spacings of the (110) and (111) planes, respectively, and the [112] orientation of the SP phase (Figure 4d). The interplanar distances in the DP phase were measured to be 2.83 and 4.63 Å, consistent with the spacings of the (220) and (111) planes, respectively, and with the [112] orientation of the DP phase (Figure 4e). Both the SP and the DP phases adopt a cubic symmetry with different crystallographic parameters. The EDX line scans and maps (Figure 5) show

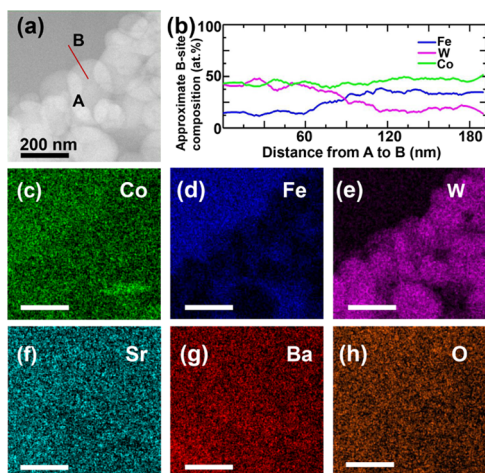


Figure 5. (a) HAADF-STEM image. (b) B-site elemental composition analysis obtained from an EDX line scan acquired from point A to point B along the red line marked in (a). (c–h) Elemental maps of Co, Fe, W, Sr, Ba, and O, respectively.

that the DP crystallites (bright) are rich in W and deficient in Fe, while the SP crystallites (dark) are characterized by a substantial enrichment in Fe and a nearly complete depletion of W. All other elements, i.e., Ba, Sr, Co, and O, are distributed homogeneously in the SP and DP crystallites. The uneven Fe and W elemental distribution is also supported by EDX elemental analysis data (Table S1, Supporting Information). The Fe and W gradients in the SP/DP composite, as well as the good structural compatibility of the phases, are favorable

for temperature-driven Fe and W interdispersion along the SP/DP heterointerface, cation redistribution, and a self-reorganized SP and DP microstructure.

In situ high-temperature XRD (HT-XRD) analysis of BSCFW0.35 was carried out. Based on the XRD patterns recorded during heating and cooling (Figure S3, Supporting Information), the mass ratios of SP and DP in BSCFW0.35 were determined as a function of temperature and are shown in Figure 6. In the temperature range between room temperature

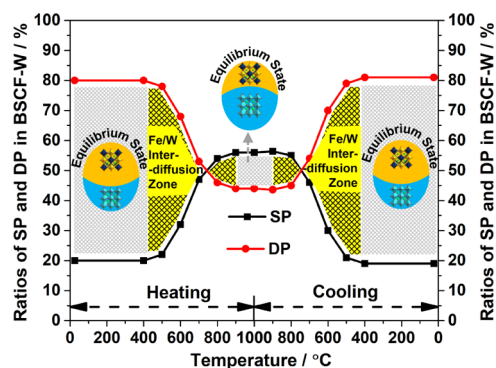


Figure 6. Temperature dependence of the mass ratios of the SP and DP phases in the BSCFW0.35 composite determined from Rietveld structure refinement.

and 400 °C, the SP and DP mass ratios were constant at approximately 20 and 80%, respectively, corresponding to a phase equilibrium state zone. The proportion of SP grew gradually with increasing temperature, reaching approximately 54% at 800 °C, while the proportion of DP decreased correspondingly to 46% as a result of a temperature-induced SP/DP interaction zone in the temperature range between 500 and 800 °C. Based on high-resolution transmission electron microscopy (HR-TEM) studies, this interaction may originate from temperature-driven Fe and W interdiffusion between the Fe-rich SP and W-rich DP phases. At temperatures above 900 °C, the ratio of the SP and DP phases was almost unchanged and stable at 44 and 56%, respectively, corresponding to a new phase equilibrium state zone. Such a change in the behavior of the mass ratios of the SP and DP phases was thermodynamically reversible with cooling from 1000 °C to room temperature. The waxing and waning of the SP and DP mass ratios in BSCFW0.35 between 500 and 800 °C represents a reversible temperature-induced SP–DP interaction, which results in a self-reorganization in phase composition to adapt to a new thermodynamic equilibrium state. As a result of this reversible temperature-induced transformation, the undesired structural distortion of the cubic SP phase in BSCFW at intermediate temperatures is restricted effectively, thereby retaining its cubic symmetry in the composite (Figure 3).

Based on the above SEM, HR-TEM, and HT-XRD studies of the BSCFW composites, the phase stabilization mechanism of the BSCFW SP/DP composite at intermediate temperatures can be inferred. The as-prepared BSCFW is a hybrid composite material, which consists of Fe-rich SP and W-rich DP phases. At low temperature, this SP–DP coexisting system is in thermodynamic equilibrium. On reaching intermediate temperatures (e.g., 600 °C), when cubic SP decomposition is expected to take place and to break the original SP–DP phase equilibrium state, the coexisting DP phase interacts with the SP phase to limit its phase distortion by means of a temperature-

driven W/Fe interdiffusion at the SP/DP heterointerface until a new SP–DP equilibrium state is reached.⁹ Any temperature variation in the intermediate temperature window results in changes in chemical compositions, as well as the mass ratio of the SP and DP phases, thereby resulting in a structural reorganization to form a new stable perovskite–fluorite composite system. The high phase stability of the BSCFW SP/DP composite at intermediate temperatures is therefore ascribed to the temperature-induced structural reorganization involving W and Fe elemental interdiffusion between the SP and DP phases, with a dynamic adjustment in the chemical composition to limit structural distortions, accompanied by new phase formation.

Oxygen Permeation Performance of the BSCFW Composite Membrane. The oxygen permeation performances of BSCF and BSCFW as oxygen-transport membranes for air separation were investigated under air/Ar oxygen partial pressure gradient conditions. As shown in Figure 7, the oxygen

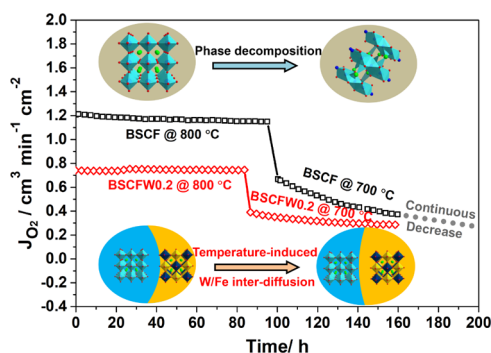


Figure 7. Oxygen permeation fluxes of BSCF and BSCFW0.2 membranes as a function of time at 800 and 700 °C. Feed side: $F_{\text{air}} = 150 \text{ cm}^3 \text{ min}^{-1}$; permeate side: $F_{\text{Ar}} = 50 \text{ cm}^3 \text{ min}^{-1}$; and thickness: 1 mm.

permeation flux of the BSCFW0.2 composite membrane at 800 °C remained stable at $0.75 \text{ cm}^3 \text{ min}^{-1} \text{ cm}^{-2}$, with no attenuation for nearly 90 h, indicating the formation of a SP–DP equilibrium state at 800 °C. Under the same conditions, the BSCF membrane exhibited a performance degradation of approximately 6% in 100 h, which was explained by the formation of the hexagonal phase, which is a bad ionic conductor.^{29,30} The performance degradation of the BSCF membrane became much more serious at 700 °C, reaching nearly 50 % (from 0.67 to $0.37 \text{ cm}^3 \text{ min}^{-1} \text{ cm}^{-2}$ after ~60 h) and increasing even further over time. In contrast, the oxygen permeation flux of the BSCFW0.2 composite membrane tended toward a plateau, with a new SP–DP equilibrium state forming after a short period of structural self-reorganization induced by switching from 800 to 700 °C, confirming its high intermediate-temperature phase stability. This was again demonstrated by the stable performance of the BSCFW0.35 composite membrane under 800 and 700 °C (Figure S4, Supporting Information). We conclude that the undesired oxygen permeation performance degradation of the BSCFW SP/DP composite membrane at intermediate temperatures due to cubic SP phase decomposition can be inhibited effectively by the temperature-induced structural reorganization of the SP/DP phases, making the self-assembled BSCFW dual-phase membrane materials very competitive for practical industrial applications.

It should be noted that the oxygen permeation flux of the BSCFW composite membranes was lower than that of the BSCF membranes, perhaps because DP oxides are usually poor conductors of oxygen ions when compared with SP oxides, even though they contain many oxygen vacancies.^{31,32} Nevertheless, for the practical application of membrane technology, stability is more important than oxygen permeability. Furthermore, the oxygen permeation flux of the BSCFW0.2 membrane was higher than that of several typical oxygen-transport membranes (Table S2, Supporting Information), showing great promise for air separation. According to the Wagner equation,³³ the oxygen permeation flux of the BSCFW composite membrane can be improved by increasing either the operating temperature or the oxygen partial pressure gradient across the membrane, as shown in Figure S5.

CONCLUSIONS

To overcome the performance degradation due to the structural deterioration in the prototypical BSCF perovskite as an oxygen-transport membrane for air separation at intermediate temperatures from 500 to 850 °C, new membrane materials $\text{Ba}_{0.5}\text{Sr}_{0.5}(\text{Co}_{0.8}\text{Fe}_{0.2})_{1-x}\text{W}_x\text{O}_{3-\delta}$ (BSCFW) consisting of Fe-rich single perovskite (SP) and W-rich double perovskite (DP) phases were developed using a one-step calcination process. In contrast to BSCF, the SP and DP coexisting dual-phase composite exhibits a high structural stability at 800 °C. Characterizations using HT-XRD, SEM, and HR-TEM reveal that the stability of the BSCFW composite is associated with a temperature-induced SP–DP dynamic interaction involving W and Fe elemental interdiffusion between the SP and DP phases. The interdiffusion of W and Fe dynamically adjusts the chemical composition and limits the structural distortion of the cubic perovskite and new phase formation. With this property, BSCFW exhibited a much more stable performance as an oxygen-transport membrane when compared to BSCF, in terms of oxygen permeation flux as a function of time at 800 and 700 °C, showing great promise for BSCFW as an intermediate-temperature oxygen-transport membrane for air separation and providing insight for designing new thermally stable composite oxides.

ASSOCIATED CONTENT

Supporting Information

The Supporting Information is available free of charge on the ACS Publications website at DOI: 10.1021/acs.chemmater.9b02213.

Original XRD results of quantitative Rietveld analysis; low-magnification HAADF-STEM images of BSCFW0.35; in situ X-ray diffraction patterns of BSCFW0.35; oxygen permeation fluxes of BSCFW0.35 membrane as a function of time; the effect of operating temperature and oxygen partial pressure on oxygen permeation flux of BSCFW0.35 membrane; elemental analysis data of the DP and SP phases in BSCFW0.35; and oxygen permeation flux comparison of BSCFW0.2 membrane with other typical OTMs (PDF)

AUTHOR INFORMATION

Corresponding Authors

*E-mail: w.a.meulenberg@fz-juelich.de (W.A.M.).

*E-mail: jianghq@qibebt.ac.cn (H.J.).

ORCID 

Heqing Jiang: 0000-0001-8964-1311

Author Contributions

#G.H. and Q.L. contributed equally.

Notes

The authors declare no competing financial interest.

ACKNOWLEDGMENTS

This research was supported financially by the National Natural Science Foundation of China (Grant Nos. 21506237 and 21536005), the International Partnership Program of the Chinese Academy of Sciences (Grant No. 153937KYSB20180048), and the Grant of DICP&QIBEBT UN201708. G.H. is grateful for support from the “Youth Innovation Promotion Association Chinese Academy of Sciences Grant 2018245” and the “2016 Jülich-OCPC-Program”. The authors thank Lidia Kibkalo for FIB preparation of the TEM specimen

REFERENCES

- (1) Wei, Y.; Tang, J.; Zhou, L.; et al. One end-dead perovskite hollow fiber membranes for high-purity oxygen production from ambient air. *Chem. Eng. J.* **2012**, *183*, 473–482.
- (2) Tan, X.; Liu, Y.; Li, K. Mixed conducting ceramic hollow-fiber membranes for air separation. *AIChE J.* **2005**, *51*, 1991–2000.
- (3) Jiang, H.; Cao, Z.; Schirmer, S.; et al. A coupling strategy to produce hydrogen and ethylene in a membrane reactor. *Angew. Chem., Int. Ed.* **2010**, *49*, 5656–5660.
- (4) Chen, Y.; deGlee, B.; Tang, Y.; et al. A robust fuel cell operated on nearly dry methane at 500 °C enabled by synergistic thermal catalysis and electrocatalysis. *Nat. Energy* **2018**, *3*, 1042–1050.
- (5) Dong, X.; Jin, W.; Xu, N.; et al. Dense ceramic catalytic membranes and membrane reactors for energy and environmental applications. *Chem. Commun.* **2011**, *47*, 10886–10902.
- (6) Jung, J.-I.; Misture, S. T.; Edwards, D. D. Oxygen stoichiometry, electrical conductivity, and thermopower measurements of BSCF ($\text{Ba}_{0.5}\text{Sr}_{0.5}\text{Co}_x\text{Fe}_{1-x}\text{O}_{3-\delta}$, $0 \leq x \leq 0.8$) in air. *Solid State Ionics* **2010**, *181*, 1287–1293.
- (7) Baumann, S.; Serra, J. M.; Lobera, M. P.; et al. Ultrahigh oxygen permeation flux through supported $\text{Ba}_{0.5}\text{Sr}_{0.5}\text{Co}_{0.8}\text{Fe}_{0.2}\text{O}_{3-\delta}$ membranes. *J. Membr. Sci.* **2011**, *377*, 198–205.
- (8) Bouwmeester, H. J. M. Dense ceramic membranes for methane conversion. *Catal. Today* **2003**, *82*, 141–150.
- (9) Mueller, D. N.; De Souza, R. A.; Yoo, H.-I.; et al. Phase stability and oxygen nonstoichiometry of highly oxygen-deficient perovskite-type oxides: A case study of $(\text{Ba,Sr})(\text{Co,Fe})\text{O}_{3-\delta}$. *Chem. Mater.* **2012**, *24*, 269–274.
- (10) Wang, F.; Nakamura, T.; Yashiro, K.; et al. The crystal structure, oxygen nonstoichiometry and chemical stability of $\text{Ba}_{0.5}\text{Sr}_{0.5}\text{Co}_{0.8}\text{Fe}_{0.2}\text{O}_{3-\delta}$ (BSCF). *Phys. Chem. Chem. Phys.* **2014**, *16*, 7307–7314.
- (11) Yaremchenko, A. A.; Patrakeev, M. V.; Naumovich, E. N.; et al. The $p(\text{O}_2)$ -T stability domain of cubic perovskite $\text{Ba}_{0.5}\text{Sr}_{0.5}\text{Co}_{0.8}\text{Fe}_{0.2}\text{O}_{3-\delta}$. *Phys. Chem. Chem. Phys.* **2018**, *20*, 4442–4454.
- (12) Müller, P.; Störmer, H.; Meffert, M.; et al. Secondary phase formation in $\text{Ba}_{0.5}\text{Sr}_{0.5}\text{Co}_{0.8}\text{Fe}_{0.2}\text{O}_{3-\delta}$ studied by electron microscopy. *Chem. Mater.* **2013**, *25*, 564–573.
- (13) Gerthsen, D.; Meffert, M.; Störmer, H.; et al. The effect of dopants on the stabilization of the cubic BSCF phase in O_2 - and CO_2 -containing atmospheres. *ECS Trans.* **2017**, *77*, 35–39.
- (14) Ravkina, O.; Klande, T.; Feldhoff, A. Investigation of Zr-doped BSCF perovskite membrane for oxygen separation in the intermediate temperature range. *J. Solid State Chem.* **2013**, *201*, 101–106.
- (15) Yang, L.; Tan, L.; Gu, X.; et al. Effect of the size and amount of ZrO_2 addition on properties of $\text{SrCo}_{0.4}\text{Fe}_{0.6}\text{O}_{3-\delta}$. *AIChE J.* **2003**, *49*, 2374–2382.
- (16) Haworth, P.; Smart, S.; Glasscock, J.; et al. Yttrium doped BSCF membranes for oxygen separation. *Sep. Purif. Tech.* **2011**, *81*, 88–93.
- (17) Unger, L.-S.; Niedrig, C.; Wagner, S. F.; et al. Yttrium doping of $\text{Ba}_{0.5}\text{Sr}_{0.5}\text{Co}_{0.8}\text{Fe}_{0.2}\text{O}_{3-\delta}$ part I: Influence on oxygen permeation, electrical properties, reductive stability, and lattice parameters. *J. Eur. Ceram. Soc.* **2018**, *38*, 2378–2387.
- (18) Fang, S. M.; Yoo, C. Y.; Bouwmeester, H. J. M. Performance and stability of niobium-substituted $\text{Ba}_{0.5}\text{Sr}_{0.5}\text{Co}_{0.8}\text{Fe}_{0.2}\text{O}_{3-\delta}$ membranes. *Solid State Ionics* **2011**, *195*, 1–6.
- (19) Kuklja, M. M.; Kotomin, E. A.; Merkle, R.; et al. Combined theoretical and experimental analysis of processes determining cathode performance in solid oxide fuel cells. *Phys. Chem. Chem. Phys.* **2013**, *15*, 5443–5471.
- (20) Liu, Y.; Zhu, X.; Li, M.; et al. Nanoparticles at grain boundaries inhibit the phase transformation of perovskite membrane. *Nano Lett.* **2015**, *15*, 7678–7683.
- (21) Lu, H.; Cong, Y.; Yang, W. Oxygen permeability and improved stability of a permeable Zr-substituted perovskite membrane for air separation. *Mater. Sci. Eng. B* **2007**, *141*, 55–60.
- (22) Shin, J. F.; Xu, W.; Zanella, M.; et al. Self-assembled dynamic perovskite composite cathodes for intermediate temperature solid oxide fuel cells. *Nat. Energy* **2017**, *2*, No. 16214.
- (23) Chen, Y.; Shen, J.; Yang, G.; et al. A single-/double-perovskite composite with an overwhelming single-perovskite phase for the oxygen reduction reaction at intermediate temperatures. *J. Mater. Chem. A* **2017**, *5*, 24842–24849.
- (24) Chen, G.; Hu, Z.; Zhu, Y.; et al. Ultrahigh-performance tungsten-doped perovskites for the oxygen evolution reaction. *J. Mater. Chem. A* **2018**, *6*, 9854–9859.
- (25) Cheng, S.; Wang, Y.; Zhuang, L.; et al. A dual-phase ceramic membrane with extremely high H_2 permeation flux prepared by autoseparation of a ceramic precursor. *Angew. Chem., Int. Ed.* **2016**, *55*, 10895–10898.
- (26) He, G.; Hu, T.; Zhou, H.; et al. Syngas production by biogas reforming in a redox-stable and CO_2 -tolerant oxygen transporting membrane reactor. *Ind. Eng. Chem. Res.* **2017**, *56*, 10134–10141.
- (27) Baumann, S.; Schulze-Küppers, F.; Roitsch, S.; et al. Influence of sintering conditions on microstructure and oxygen permeation of $\text{Ba}_{0.5}\text{Sr}_{0.5}\text{Co}_{0.8}\text{Fe}_{0.2}\text{O}_{3-\delta}$ (BSCF) oxygen transport membranes. *J. Membr. Sci.* **2010**, *359*, 102–109.
- (28) Popov, M. P.; Starkov, I. A.; Bychkov, S. F.; et al. Improvement of $\text{Ba}_{0.5}\text{Sr}_{0.5}\text{Co}_{0.8}\text{Fe}_{0.2}\text{O}_{3-\delta}$ functional properties by partial substitution of cobalt with tungsten. *J. Membr. Sci.* **2014**, *469*, 88–94.
- (29) Li, X.; Kerstiens, T.; Markus, T. Oxygen permeability and phase stability of $\text{Ba}_{0.5}\text{Sr}_{0.5}\text{Co}_{0.8}\text{Fe}_{0.2}\text{O}_{3-\delta}$ perovskite at intermediate temperatures. *J. Membr. Sci.* **2013**, *438*, 83–89.
- (30) Liu, Y.; Zhu, X.; Yang, W. Degradation mechanism analysis of $\text{Ba}_{0.5}\text{Sr}_{0.5}\text{Co}_{0.8}\text{Fe}_{0.2}\text{O}_{3-\delta}$ membranes at intermediate-low temperatures. *AIChE J.* **2005**, *61*, 3879–3888.
- (31) Sengodan, S.; Choi, S.; Jun, A.; et al. Layered oxygen-deficient double perovskite as an efficient and stable anode for direct hydrocarbon solid oxide fuel cells. *Nat. Mater.* **2015**, *14*, No. 205.
- (32) Kim, J.; Yin, X.; Tsao, K.-C.; et al. $\text{Ca}_2\text{Mn}_2\text{O}_5$ as oxygen-deficient perovskite electrocatalyst for oxygen evolution reaction. *J. Am. Chem. Soc.* **2014**, *136*, 14646–14649.
- (33) Schroeder, M. Modeling of dense ceramic bilayer membranes. *Phys. Chem. Chem. Phys.* **2005**, *7*, 166–172.